

Effects of thin high-z layers on the hydrodynamics of laser-accelerated plastic targets.

S.P. Obenschain, D. Colombant, M. Karasik, C. J. Pawley, V. Serlin, A. J. Schmitt, J. Weaver, *Plasma Physics Division, Naval Research Laboratory, Washington D. C.*

J. H. Gardner, L. Phillips, *Laboratory for Computational Physics and Fluid Dynamics, Naval Research Laboratory , Washington DC*

Y. Aglitskiy and Y. Chan, *Science Applications International, McLean, VA*

J. P. Dahlburg, *General Atomics, San Diego, CA*

M. Klapisch, *Artep Inc, Colombia, MD*

Abstract

We present experimental results and simulations that study the effects of thin metallic layers with high atomic number (high-Z) on the hydrodynamics of laser accelerated plastic targets. These experiments employ a laser pulse with a low-intensity foot that rises into a high-intensity main pulse. This pulse shape simulates the generic

shape needed for high-gain fusion implosions. Imprint of laser nonuniformity during start up of the low intensity foot is a well-known seed for hydrodynamic instability. We observe large reductions in hydrodynamic instability seeded by laser imprint when certain minimum thickness gold or palladium layers are applied to the laser-illuminated surface of the targets. The experiment indicates that the reduction in imprint is at least as large as that obtained by a 6 times improvement in the laser uniformity. We present simulations supported by experiments showing that during the low intensity foot the laser light can be nearly completely absorbed by the high-Z layer. X-rays originating from the high-Z layer heat the underlying lower-Z plastic target material and cause large buffering plasma to form between the layer and the accelerated target. This long-scale plasma apparently isolates the target from laser nonuniformity and accounts for the observed large reduction in laser imprint. With onset of the higher intensity main pulse, the high-Z layer expands and the laser light is transmitted. This technique will be useful in reducing laser imprint in pellet implosions and thereby allow the design of more robust targets for high-gain laser fusion.

I. INTRODUCTION

The direct-drive scheme for laser fusion has potential to achieve the high-energy gains (>100) needed for fusion energy.¹ For high gain we need highly symmetric implosions, where a small portion of the DT fuel in the center is ignited, followed by a fusion burn that propagates outward through a surrounding layer of highly compressed fuel. The convergence ratio between the initial pellet radius and that of the ignited fuel dictates laser illumination and pellet uniformities of a few percent. Modern laser beam smoothing technologies can attain this basic level of target illumination uniformity.² However, hydrodynamic instability greatly increases the symmetry challenge. Very small laser illumination and target nonuniformity seeds may grow to sufficient amplitude to reduce gain or even prevent the ignition.^{3,4} This challenge has motivated efforts to improve laser and target uniformity, and to develop techniques that reduce laser imprint and that reduce the growth rates for hydrodynamic instability. In an earlier computational study of high gain pellet implosions, a high-Z layer (high-atomic-number) was employed to preheat the ablator with x-rays with the intent of reducing growth rates for hydrodynamic instability.⁵ In this paper we show that under certain circumstances, the addition of a thin high-Z layer can greatly reduce the laser imprinting onto plastic laser-accelerated targets. We examine both Pd and Au layers. This technique will be useful in designing fusion pellets that are resistant to laser imprint.

The experiments described here employ the Nike Krypton-Fluoride (KrF) laser facility⁶ to accelerate planar plastic targets with and without high-Z and low-Z metallic layers using 248 nm light. This facility can achieve a highly uniform illumination on

target with root-mean square (RMS) nonuniformity $<0.2\%$ when averaged over 4 ns for spatial wavelengths relevant to hydrodynamic instability in our targets ($\lambda=10\text{-}100\text{ }\mu\text{m}$). We use a laser pulse with a relatively low intensity foot ($\sim 2\text{-}3 \times 10^{12}\text{ W/cm}^2$) that initially compresses the targets followed by a higher intensity main pulse that accelerates the targets. Pulse shapes with a low intensity foot ($\sim 10^{12} \text{ --- } 10^{13}\text{ W/cm}^2$) are needed for high gain targets to set the proper adiabat for the pellet compression. Simulations have shown that laser imprint occurs primarily during the low intensity foot pulse.^{7,8} A long scale buffering plasma forms during the higher intensity main pulse that smoothes the effects of laser illumination nonuniformity. The relatively cold (50-100eV) plasma that forms during the foot pulse does not have sufficiently good electron thermal conductivity between the target and the laser absorption region to allow such long scale plasmas to form. X-radiation from a high-Z layer provides an alternative means for energy transport from laser absorption to target, and allows a long scale buffering plasmas to form during the low intensity foot pulse.

Earlier experiments and simulation studies have explored means to reduce laser imprint by the target configuration and showed the promise of this approach. This includes work with high-Z layers on aluminum targets⁹, the use of low density foams¹⁰, the use of external x-rays before the laser pulse to create a plasma¹¹, the use of foams preheated by x-rays^{12,13,14,15, 16} and use of a high—Z layer on the plastic membrane of a cryogenic deuterium-loaded-foam targets.¹⁷ The most extensive experimental work has involved use of a low-density plastic foam layer that is heated by x-rays from a thin high-Z layer during the initial portion of the laser pulse. The goal here is to have an x-ray driven supersonic ionization wave through the foam that produces a buffering plasma.

This configuration has been shown to reduce instability-amplified laser imprint using 527-nm and 337-nm laser light. However, it is challenging to produce foams of suitable low density and sufficient uniformity, and there is the potential for hydrodynamic instability at the interface between the foam and the higher density target. The work presented here suggests that the foam is not essential and the configuration of high-Z layer on conventional plastic also works well at reducing imprint.

Experimental work presented here on imprint mitigation is in particular distinguished from earlier work on imprint mitigation by two factors, (1) the use of pulses with a low intensity foot and (2) the use of higher laser illumination uniformity.

(1) We make use of a pulse shape in the experiment that simulates the one needed by a high gain target (low intensity foot in the intensity range needed for high-gain pellets, followed by the main pulse). Most of the previous experimental studies have used a fast rising rectangular laser pulse with peak intensities above 10^{14} W/cm². The imprinting, laser absorption characteristics and the radiation from laser-illuminated targets are sensitive to the incident laser intensity. The x-radiation spectrum will harden at higher laser intensities and change depth of penetration in the target. A smoothing technique that works well at one intensity and pulse shape may not work well at another. In our configuration we choose high-Z layers that are thick enough to absorb most of the laser light during the low intensity foot, but thin enough for the laser to bleach through the high-Z layer at higher intensities ($\geq \text{few} \times 10^{13}$ W/cm²). This allows efficient direct-drive during the main pulse. We would not expect this particular configuration and choice of high-Z layer thickness to work well at imprint mitigation with rectangular shaped higher intensity pulses. Our pulse shaping is also essential to account for the potentially

unstable radiation-hydrodynamics in the transition from the foot pulse to the main pulse.¹⁸

(2) Our studies include the use of extremely uniform laser irradiation of targets. This uniform illumination allowed us to observe a potentially deleterious effect of the high-Z layers that otherwise would have been missed. We found for the case of a too thin high-Z layer and our best laser illumination uniformity that there is enhanced nonuniformity in the accelerated targets. These very thin layers apparently are unstable during the initial expansion from the target and introduce modulations in the laser intensity producing target nonuniformity. The seed for this instability is apparently small nonuniformity in the high-Z layer. This effect is masked by laser imprint when we use less uniform illumination. This deleterious effect is eliminated in our experiments by use of a thicker high-Z layer.

We present laser imprint studies where the target illumination uniformity during the foot is varied by forming the foot from either 1 or 39 overlapped laser beams. Measurements of the effects of this large variation in illumination uniformity on the target stability allowed us to calibrate the level of improvement when using the high-Z layers. The effect of a high-Z layer under some circumstances was larger than that obtained with the 39× increase in number of overlapped beams. We provide simulations and experimental measurements that indicate that one can achieve an effectively indirect-drive configuration^{19,20} during the foot pulse where the target is driven by x-rays emitted by the high-Z layer. The laser light during the foot is absorbed in the high-Z layer (if it is sufficiently thick) and x-ray emission from the layer heats the underlying lower-Z material from the target that quickly pushes the layer >100 μm from the target surface.

We believe that the large buffering plasma is the primary reason for the observed reduction in hydrodynamic instability seeded by imprint. However, we also observe delays in growth to saturation of hydrodynamic instability seeded by initial target nonuniformity when using the high-Z layers. There may be secondary potentially beneficial effects with the high-Z layers that will also be discussed.

II. EXPERIMENTAL ARRANGEMENT AND CONDITIONS

Figure 1 shows the experimental arrangement and the primary x-ray backlighting diagnostic. Up to 40 Nike beams are overlapped onto the targets with an overall cone half angle of ~ 13 degrees. The individual beams have a flat top of approximately 400- μm diameter and a half intensity diameter of 750 μm . For the target acceleration experiments we employed a 2-3% amplitude 3-3.5 ns foot pulse followed by a 4 ns main laser pulse. Typically the energy on target is 1600 J with peak intensity of $7 \times 10^{13} \text{ W/cm}^2$. Nike employs induced spatial incoherence (ISI) beam smoothing.²¹ ISI uses controlled incoherence to achieve uniform illumination when averaged over times long compared to the laser's 0.7 psec coherence time. Figure 2 shows a time-averaged focal distribution for a Nike beam and the calculated nonuniformity for shorter averaging times. The residual nonuniformity is not completely smoothed out on the hydrodynamic time scales of ($\sim 100 \text{ ps}$), and is the source for laser imprint. For all the data shown here the main laser pulse was formed by overlapping 39 Nike beams. The foot pulse was formed in two ways. For the most uniform target illumination all 39 overlapped beams had a pulse shape with the desired foot pulse. To achieve approximately $6\times$ less uniform

illumination during the foot, we employed 39 main beams with a 4-ns rectangular pulse shape, and the foot was formed by using a single auxiliary laser beam whose leading edge arrived 3 ns earlier than the other 39 beams.

We used 40- μm ($\pm 1 \mu\text{m}$) thick polystyrene targets for the experiments. The flat targets typically have surface finishes of better than 50 μm rms as measured by white-light interferometry. This high target quality is needed to ensure that laser rather than target nonuniformity dominates in our imprint studies. A portion of the targets were coated on the laser illuminated side by thin (100 -1200 \AA) metallic layers of palladium, gold or aluminum. The high-Z layers are typically uniform to within a few percent over spatial wavelengths $\geq 15\mu\text{m}$ (as determined by spatially-resolved light transmission measurements through the coated foils).

We used a number of diagnostics to characterize the laser target interaction. We image the rear surface of the accelerated targets onto an optical streak camera to monitor target preheat and shock breakout times. A soft x-ray (100-1000 eV) spectrometer with time resolution and harder x-ray detectors (1.5-10 keV) measured the x-ray emission. Visible and IR detectors monitor early time heating by the laser pulse. Side-on x-ray backlighting using a Si source and a streak camera was used to determine typical acceleration histories. These sidelighting measurements indicated that the uncoated plastic laser-accelerated targets travel a nominal 230 μm by the end of the 4-ns main pulse. We observed some reduction in the target displacement with Au and Pd layers of thickness sufficient to reduce imprint. The measurements indicated that there was a delay of acceleration in the targets of about 0.5 ns apparently due to the presence of the

buffering plasma. As discussed in section IV, this effect is too small to account for the observed reduction in Rayleigh-Taylor (RT) amplified imprint.

Like in many other experiments that have studied laser imprint,^{22,23,24} the primary diagnostic used in our experiment is face on x-ray backlighting that detects areal mass nonuniformity in the accelerated targets. X-rays from a laser illuminated Si source transmit through the target and are imaged onto the slit of an x-ray streak camera by means of a spherical quartz crystal.²⁵ (See Fig. 1.) The crystal selects the 1.86 keV Si line emission by Bragg diffraction and thereby discriminates heavily against self-emission from the laser-accelerated target. This high contrast is particularly needed when using the targets with metallic layers. Data was taken with magnifications of 20× and 30×. The modulation transfer function (MTF) with 30× magnification is approximately 55% at for 30 μm wavelength and 35% at 20-μm wavelength. Earlier work²⁶ using similar conditions and a high spatial resolution x-ray framing camera showed that the instability-amplified imprint initially appeared with the spectrum peaked near 20-μm wavelength early in time, and then evolved into longer wavelength modes with saturation.

III. LASER IMPRINT WITH AND WITHOUT METALLIC LAYERS

Figure 3 shows 2-dimensional calculations (using the NRL FAST code²⁷) of laser imprint with our experimental conditions. Shown is the expected evolution of the imprint when using a foot formed by a single beam (a) and 40 beams (b) onto uncoated plastic targets. The calculation accounts for all the modes in an ISI smoothed single beam. For

the multibeam foot the calculation reduces the nonuniformity on target by the square root of the number of beams, $(40)^{-1/2} \cong 0.16$, which is expected from the statistical averaging when one ignores the very short scale ($\lambda < 7\mu\text{m}$) nonuniformity arising from overlapping beams at angles. The computer-generated streak-camera images show the evolution of areal mass nonuniformity in the targets that is seeded by laser imprint. With the single beam foot, a large amplitude areal mass nonuniformity is predicted by the middle of the main 4 ns laser pulse. The RMS amplitude reaches 1 mg/cm^2 (25% of the initial target areal mass) by 2.3 ns. (Time zero here and for all of the results presented in the paper corresponds to the 50% rise of the main pulse.) The instability amplified imprint from the multibeam foot is lower and reaches the 25% level at 4 ns, 1.7 ns later than with the single beam foot.

We now present results from the experiments that study the growth of hydrodynamic instability seeded by laser imprint with and without a metallic layer on the laser illuminated surface. Figure 4 shows experimental data using a single-beam foot onto a plain plastic target. It includes an image of areal mass nonuniformity calculated from the streak camera image of x-rays transmitted through the target, and lineouts showing the evolution of areal mass nonuniformity in the accelerated target. The areal mass nonuniformity is calculated from the spatial variations in the 1.86 keV x-rays transmitted through the target. Both the streak image and the lineouts are corrected for the imaging system's MTF for wavelengths of $20\mu\text{m}$ and longer. With the single beam foot, we observe growth in the areal mass nonuniformity to a peak-to-valley variation equal to the initial target thickness (4 mg/cm^2) by 1.5 ns and reaching 6 mg/cm^2 by 2 ns. (The high-

density spikes in the nonlinear stages of Rayleigh-Taylor growth allow areal mass nonuniformity amplitudes larger than the initial areal mass of the target.)

Figure 5 shows experimental results for a foot pulse formed by 39 beams. The imprint seed for instability is expected to be smaller due to the statistical $(39)^{-1} = 6.3 \times 10^{-3}$ improvement in effective illumination uniformity; and we do observe a delay in the onset of measurable areal mass nonuniformity. The areal mass nonuniformity just reaches a peak-to-valley amplitude of 4 mg/cm^2 by the trailing edge of the main laser pulse ($t=4\text{ns}$).

Figure 6 shows the experimentally observed areal mass nonuniformity when using a single beam foot with a 1200 Å Pd layer on the laser-illuminated surface. There is no measurable mass nonuniformity above the noise in the diagnostic throughout the target acceleration. The improvement in accelerated target uniformity with the Pd layer is better than that observed with increased number of beams in Figure 5 .

Figure 7 shows growth in the RMS areal mass nonuniformity as a function of time for the cases given in Figs. 4 to 6. With Pd the areal mass modulation never rises above the noise ($\sim 0.2 \text{ mg/cm}^2$) in the diagnostic. The growth in the RMS level for the case of the 39-beam foot onto plain plastic is in good agreement with the simulations of Fig. 3. However, the single beam imprint onto plain plastic rises to saturation about 1-ns earlier than the simulation. This disagreement with the single beam imprint may reflect physics effects not included in the simulation (such as nonlinear refractive and laser-plasma coupling).

Figure 8 is a gallery of typical images of areal mass uniformity that was observed when using a single beam foot pulse and different metallic layers (600 Å and 100 Å Au, 400 Å Pd, and 1200 Å Al). The case of a 600 Å Au layer shown in Figure 8 gives a

similar result to that obtained with 1200 Pd in Fig.6, with no measurable areal mass nonuniformity from imprint. The Au layers were observed to reduce the effects of laser imprint with thicknesses down to about 300 . With a layer thickness near 100 , the gold was observed to have no beneficial effect on imprint with a single beam foot. Palladium layers of 800 were observed to reduce imprint-seeded nonuniformity; while a 400 Pd layer allows imprint as evident from the streak camera image in Fig. 8. (Note that gold has about twice the mass density as palladium, so both the metals are effective at reducing imprint with layers that have about equal areal mass densities.) A layer consisting of 1200 of Al did not appreciably change the laser imprint.

Figure 9(a) shows a streaked image of the growth of the areal mass nonuniformity for the case of a 39-beam foot pulse with a 95 Au layer. We observe modulations with characteristic spatial structures of longer wavelength than that observed with laser-imprint onto plain CH. Framing camera images show development of a honeycomb-like structure in the areal mass density with such Au layers. Fig 9 (b) shows growth of the RMS areal mass modulation with and without the 95 Au layer. Here, with a more uniform illumination than in Fig. 8, we see a clear enhancement of areal mass nonuniformity with the addition of the 95 Au layer. Our simulations indicate that thin Au layers can be Rayleigh-Taylor unstable as the underlying lower density CH plasma expands against and accelerates the higher density Au layer. Modulations in the Au thickness can then modulate the laser intensity. The seed for this effect is likely initial nonuniformity in the gold layer.

IV. MECHANISMS FOR THE REDUCED INSTABILITY WITH HIGH-Z LAYERS.

We observe a large decrease in the imprint-seeded hydrodynamic instability when using Au or Pd layers of sufficient thickness. There are various mechanisms that can come into play to achieve this result. We expect some reduction in Rayleigh-Taylor growth due to the observed reduction in target displacement with the thicker high-Z layers due to delay in the target acceleration by the buffering plasma. The corresponding delay in onset of measurable RT-amplified growth would be only 0.5 ns and is too small to explain the observations. Another possibility is heating of the target by x rays with a concomitant reduction in the instability growth rates due to the reduction in the target density. We examine these mechanisms by looking at the effects of the high-Z layers on growth from targets that are initially perturbed by a sinusoidal mass nonuniformity. We observe that while there is a delay in growth to saturation, the experiment is not consistent with bulk heating of the target with the high-Z layers. We conclude based on simulations and our experimental evidence discussed below, that the primary cause of the reduction in the target's nonuniformity is actual reduction in the laser imprint during the foot pulse.

Figure 10(a) shows images for targets with an initial 60 μm wavelength and 0.125 μm amplitude sinusoidal ripple on the laser illuminated surface. Shown are results for the cases of: a single beam foot and a 39-beam foot onto plain plastic targets, and a single beam foot and a plastic target with an 800 μm Pd layer. The imprint obscures growth of the 60- μm mode with the single beam foot and there is some competing imprint with the

39-beam foot. The 60- μm mode dominates with the Pd layer. Figure 10(b) shows growth of the predominant 60- μm mode for the case of the plastic only (with multibeam foot) and the Pd-coated target. The mode without the Pd grows about 400 psec earlier. However the growth rates towards saturation are similar. This result may be completely accounted for by the observed short delay in target acceleration with the thicker high-Z layers. See Fig. 10(c), which shows the distance the target rear surface has traveled as a function of Pd thickness (as determined by x-ray sidelighting measurements). Analysis of the trajectories indicates that the reduction in distance traveled with increased Pd thickness reflects primarily a delay in the time of target acceleration by the main pulse by up to ~ 0.5 ns.

Figure 11(a) shows similar results for various thickness Au layers where the instability growth is seeded by a 30- μm wavelength by 0.125 μm amplitude sinusoidal ripple. We again observe a delay in growth to saturation that increases with the thicker Au layers. Figure 11(b) shows the growth of the 30- μm modes where the data with a 420 Au layer is time shifted 1.2 ns earlier. The time evolution is very similar for the time-shifted data with the Au layer and the uncoated plastic target.

The results with the rippled targets show a delay, but no distinct effects on the growth rates for the sinusoidal modes at the times in the laser pulse that we can observe them. The delay in target acceleration can explain a portion of this effect. In addition, the early time heating from soft x-rays should be softening the density profiles in the ablation regions and may be altering the establishment of the Rayleigh-Taylor eigenmodes. This later effect may account for larger delay observed in the data shown in Fig. 11 (Au layer and shorter wavelength $\lambda=30$ μm mode). However, the results in Figures 10 and 11

indicate that x-rays are not preheating the targets enough to affect later time Rayleigh-Taylor growth rates.

Figure 12(a) and 12(b) show time-resolved measurements of x-ray emission from the laser-illuminated surface of our targets. Figure 12(a) shows the spectra of soft x-rays emitted during the foot pulse. For Pd or Au layers that are sufficient to reduce imprint, the x-ray spectra <500 eV are of similar intensity. The x-rays during the foot are of too low energy <1 keV to penetrate through the targets and cause bulk preheat. Figure 12(b) shows the time history of harder x-ray emissions measured by a diode filtered to accept x-rays above 1.5 keV. These harder x-rays generated during the main pulse can penetrate through the interior of the plastic targets. For both Au and Pd layers we observe a short burst of hard x-rays as the main pulse ramps up, but the signal falls to near that of the plastic targets before the end of the pulse. The peak signal from the Pd coated target represents a conversion efficiency (laser into hard x-rays) of about 0.2%. We calculate that this amount of hard x-rays cannot appreciably heat our targets beyond what they experience by the shock waves.

The observed effects on the instability growth with rippled targets (~ 0.5 -1 ns delay in growth to saturation) is too small to explain the total absence of measurable imprint when we use the thicker Au and Pd layers and a single beam foot. Measurable imprint appears with the uncoated plastic targets within the first ns of the main drive pulse, yet we cannot observe imprint 3 ns later with the high-Z layers. It thus appears that the laser imprint is indeed being reduced. The mechanism is the production of large buffering plasma by x-rays from the high-Z layer. We discuss below measurements and simulations that support this as the mechanism.

Figure 13 shows side-on measurements of soft x-rays emitted by targets with and without Au layers. The streak camera cathode was filtered by a 1 μm polyamide foil that was coated by 1000 \AA Al. This arrangement is sensitive to soft x-rays emitted during the foot pulse. For these experiments we used a longer foot pulse (4ns), thicker targets (100 μm) than used in the imprint experiments. The sequence shows side-on target emission from plain plastic targets and targets with 200 \AA and 400 \AA Au layers. For the plain CH, the emission is concentrated within 20-30 μm of the target surface during the foot pulse. For the 200 \AA Au layer the emission from the Au layer dominates, but we also observed emission in the region between the layer and the solid target surface. The measurements indicate that appreciable laser light is penetrating this gold layer during the foot pulse. The Au layer is apparently rapidly pushed away from the target by the underlying hot (CH) plasma from the plastic target.

For the case of the thicker 400 \AA layer, (sufficient to reduce imprinting in our experiments), there is much reduced x-ray emission from the region between the Au layer and the target during the foot pulse. This indicates that much less laser light is now penetrating the gold layer and directly heating the underlying plasma. This interpretation is supported by the behavior after the main pulse ramps up. The x-ray emission appears close to the target surface with the plain plastic and the 200 \AA Au layered target. The case with the 400 \AA layer is qualitatively different with the emission starting first from the gold layer and appearing to bleach through the plasma towards the target surface. The emission with the 400 \AA layer is consistent with the laser being primarily absorbed by the gold layer during the foot of the pulse. The distances between the Au layer and the target are too long for thermal conduction to be ablating the material from the target surface.

The most plausible mechanism for the observations is that x-rays emitted from the high-Z layer are heating and ablating material from the target surface. In effect this is x-ray drive during the foot pulse. Simulations confirm this conjecture.

Figure 14(a,b,c) shows snapshots of the calculated laser and x-ray flux, mass density and temperature of the coronal plasma at $t = -1$ ns, near the end of the foot used for target acceleration experiments. Shown are results with a plain CH target (a), with a 100 Å Au layer (b), and with a 400 Å Au layer (c). For the 400 Å Au layer, the laser is nearly completely absorbed in the Au layer that is displaced about 100 μm from the target surface. The x-ray flux in the region between the Au layer and the target surface is much larger than the laser flux. For these conditions, the energy transport into the target ablation region was found to be primarily by means of x-rays, with negligible contributions from the laser and thermal conduction. For these conditions we have x-ray driven ablation and ablation pressures. The calculated pressure applied to the target during the foot by the x-ray drive is about 50% higher than that obtained without the Au layer. With the 100 Å Au layer, the calculations show that the laser is transmitted through the Au layer, but there is still a longer scale plasma than that obtained with no Au. In all cases, even with CH, there is a region in the vicinity of the ablation layer where radiation transport dominates. With the thickest Au layer, that region is much larger. The simulation in Fig. 14(d) shows that the laser light bleaches through the (initially 400 Å) Au plasma laser early ($t = +1$ ns) in the main pulse.

With our KrF laser system, the target is bathed at low levels (about 10^7 W/cm²) for 100 ns before the foot pulse due to amplified spontaneous emission (ASE) from the large KrF amplifiers. We observe via calibrated optical and infrared pyrometry that the

high-Z layers are preheated by this early time illumination to a few tenths of an eV. This low level of illumination and preheat may have the beneficial effect of causing the layer to expand to an appreciable thickness (10 s of μm) prior to the arrival of the foot pulse and thereby providing an additional early time buffer to laser nonuniformity.

V. CONCLUSIONS

We observe large reductions in instability seeded by laser imprint when using thick enough Pd or Au layers. We believe that the main mechanism for this result is smoothing in a large buffering plasma produced by x-rays from the high Z-layers. Both simulations and experiment support this interpretation.

The results of the experiment indicate that high-Z layers should be useful for designing pellets that are resistant to the deleterious effects of laser imprint. We have studied the effects of adding thin Pd layers to direct drive target pellets designs with 1-D simulations. Figure 15 shows a sample implosion, and a plot of gains obtained verses Pd layer thickness on the pellet using a 1.5 MJ and 4 MJ KrF laser. Here the pellet configuration is similar to that described elsewhere²⁸ with a deuterium-tritium loaded foam ablator and with a high-Z layer on a thin plastic outer shell. We find that there is no gain penalty in adding the Pd layers. This work indicates that we can use high-Z layers to obtain high gain pellet designs that are more robust due to their resistance to laser nonuniformity. Multidimensional simulations to examine these targets are underway.

Acknowledgements

This work was supported by the U. S. Department of Energy, NNSA-Defense Programs. We thank the Nike laser-target crew (Dennis Brown, Laodice Granger, Del Hardesty, David Kehne, Steve Krafsig, Nick Nocerino, J. Picciotta, Zeb Smyth and Steve Terrel) for excellent support. We acknowledge very helpful discussions with John Sethian, Andrew Mostovych and Stephen Bodner. We thank Tom Walsh and Ed Hsiegh, Schafer Corp for the coated target fabrication. We thank Anita Schwendt, Los Alamos National Laboratory, for suggesting the use of Pd for the advantages it would have in diffusive filling of pellets with DT fuel.

References

- ¹ S. E. Bodner, D. G. Colombant, J.H. Gardner et al., Phys. Plasmas **5**, 1901 (1998).
- ² Joshua E. Rothenberg, J. Opt. Soc. Am. B **14**, 1664 (1997).
- ³ S. V. Weber, S. G. Glendinning, D. H. Kalantar, M.H. Key, B. A. Remington, J. E. Rothenberg, E. Wulfrum, C. P. Verdon, and J. P. Knauer, Phys. Plasmas **4**, 1978 (1997).
- ⁴ Andrew J. Schmitt, A. L. Velicovitch, J. H. Gardner, C. Pawley, S. P. Obenschain, Y. Aglitskiy, and Y. Chan, Phys. Plasmas **8**, 2287 (2001).
- ⁵ S. E. Bodner, D. B. Colombant, A. J. Schmitt, and M. Klapish, Phys. Plasmas **7**, 2298 (2000).
- ⁶ S. P. Obenschain, S. E. Bodner, D. Colombant et al., Phys. Plasmas **3**, 2098 (1996).
- ⁷ M. H. Emery, J. H. Gardner, R. H. Lehmberg, and S. P. Obenschain, Phys. Fluids **9**, 2640 (1991).
- ⁸ V.N. Goncharov, S. Skupsky, T. R. Boehly et al., Phys. Plasmas **7**, 2062 (2000)

-
- ⁹ J. L. Bocher, M. Decroisette, P. A. Holtstein, M. Louis-Jacquet, B. Meyer, A. Saleres, and G. Thiell, Phys. Rev. Lett **52**, 823 (1984).
- ¹⁰ Nathan Metzler, Alexander Velikovitch, and John H. Gardner, Phys. Plasmas **8**, (1999)
- ¹¹ M. Desselberger, T. Afshar-rad, F. Khattak, S. Vianna, and O. Willi, Phys. Rev. Lett. **68**, 1539 (1992).
- ¹² M. Desselberger, M.J. Jones, J. Edwards, M. Dunne, and O. Willi, Phys. Rev. Lett, **74**, 2961 (1995)
- ¹³ R. G. Watt, J. Duke, C. J. Fontes, P. L. Gobby, R. V. Hollis, P. A. Kopp, R. J. Mason, and D. C. Wilson, Phys. Rev. Lett. **23**, 4644 (1998).
- ¹⁴ M. Dunne, M. Borghesi, A. Iwase et al., Phys. Rev. Lett. **75**, 3858 (1995)
- ¹⁵ H. Nishimura, H. Shiraga, H. Azechi et al., Nuclear Fusion **40**, 547 (2000)
- ¹⁶ R. J. Mason, R. A. Kopp, H. X. Vu et. al, Phys. Plasmas **5**, 211 (1998).
- ¹⁷ J.D. Sethian, S. E. Bodner, D. G. Colombant et al., Phys. Plasmas **6**, 2089 (1999)
- ¹⁸ J. P. Dahlburg, M. Klapish, J. H. Gardner, C. R. Devore, A. J. Schmitt and A. Bar-Shalom, J. Quant. Spectros. Radiat. Transfer **54**, 113 (1995).
- ¹⁹ John Lindl, Phys. Plasmas **2**, 3933 (1995).
- ²⁰ S. Eliezer, J. J. Honrubia and G. Verlarde, Phys. Lett A **166**, 249 (1992).
- ²¹ R. H. Lehmberg and J. Goldhar, Fusion Technol. **11**, 532 (1987).
- ²² R. J. Taylor, J. P. Dahlburg, A. Awase, J. H. Gardner, D. E. Fyfe and O. Willi, Phys. Rev. Lett **76**, 1643 (1996).
- ²³ S. G. Glendinning, S. N. Dixit, B. A. Hammel, et. al, Phys. Rev. Lett **80**, 1904 (1998).
- ²⁴ V. A. Smalyuk, T. R. Boehly, D. K. Bradley, et al., Phys. Rev. Lett **81**, 5342 (1998).
- ²⁵ Y. A. Aglitskiy, T. Lehecka, S. Obenschain et al., Appl. Opt. **37**, 5261(1998).

²⁶ C. J. Pawley, K. Gerber, R. H. Lehmberg et al., Phys. Plasmas **4**, 1969 (1997).

²⁷ John H. Gardner, Andrew J. Schmitt, Jill P. Dahlburg et al., Phys. Plasmas **5**, 1935 (1998).

²⁸ S. E. Bodner, D. B. Colombant, A. J. Schmitt, and M. Klapish, Phys. Plasmas **7**, 2298 (2000).

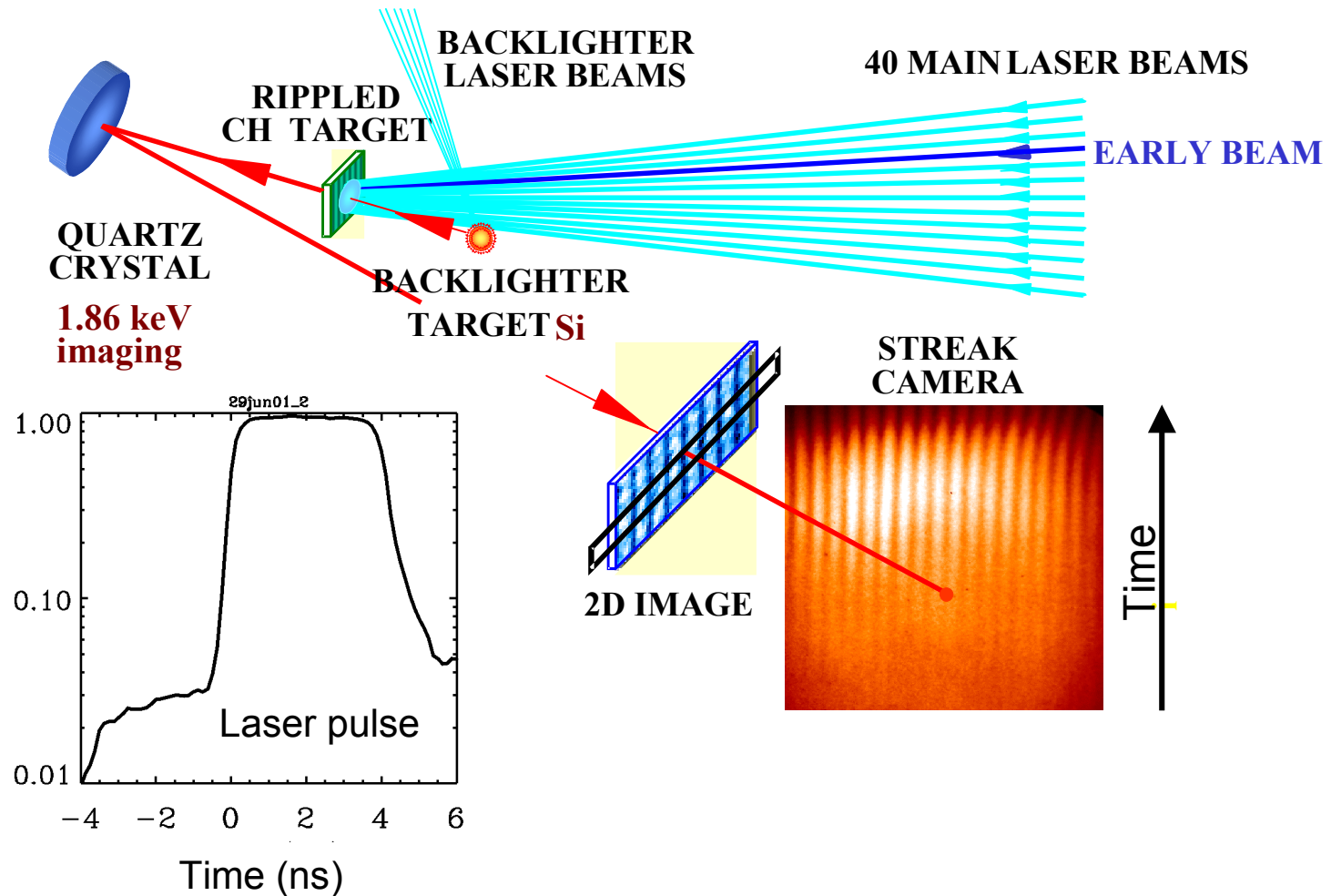


Figure 1. Areal mass nonuniformity in laser-accelerated targets is detected by monochromatic x-ray backlighting using spherical quartz crystal optics to select the 1.86 keV line from the laser-illuminated Si backlighter target. Shown is the case of an initially rippled plastic target (CH); most of the data presented here is with initially smooth targets where laser imprinting causes the observed target nonuniformity. The laser pulse has a ~3 ns low intensity foot that can be formed by all the overlapped beams, or a single laser beam that arrives 3 ns early.

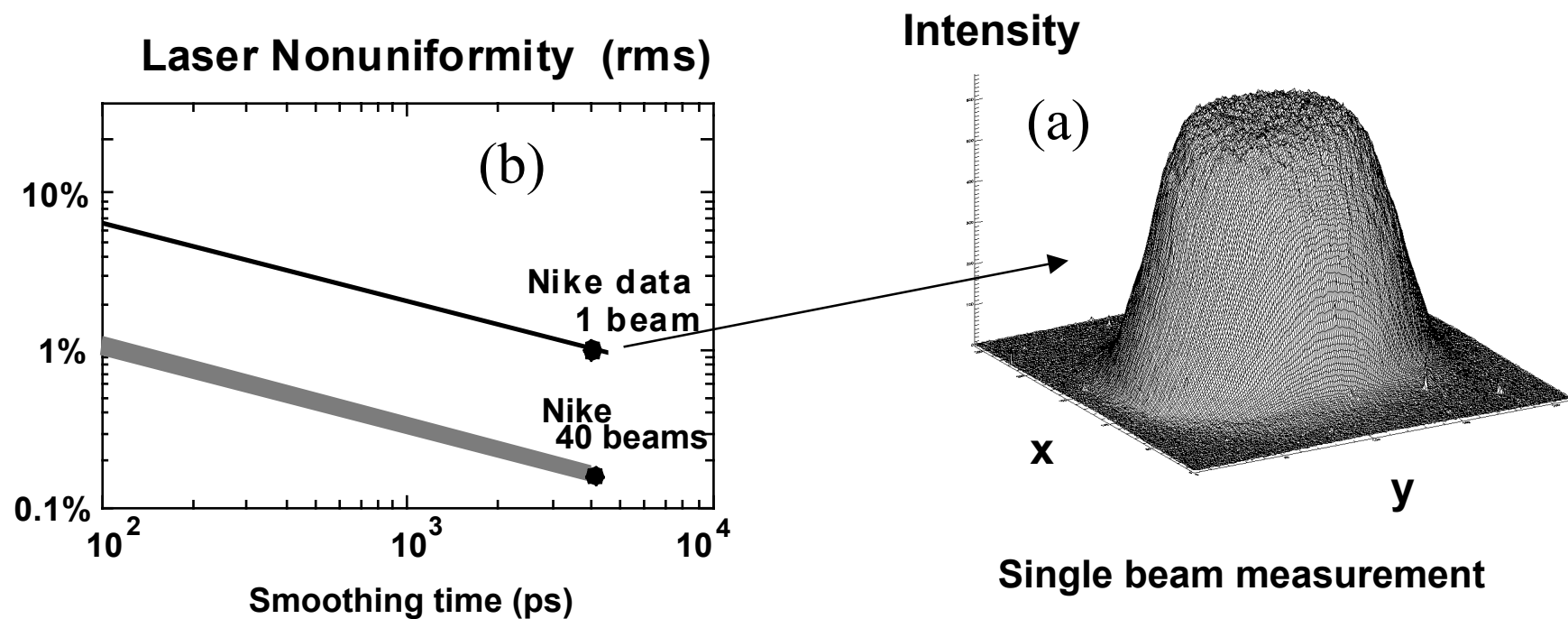


Figure 2. (a) Measured focal profile for a single 4-ns duration high-energy Nike laser beam, and (b) the calculated RMS illumination nonuniformity for a single beam and the effective nonuniformity for 40 overlapped laser beams. The uniformity improves as the square root of the time over which one averages the profile.

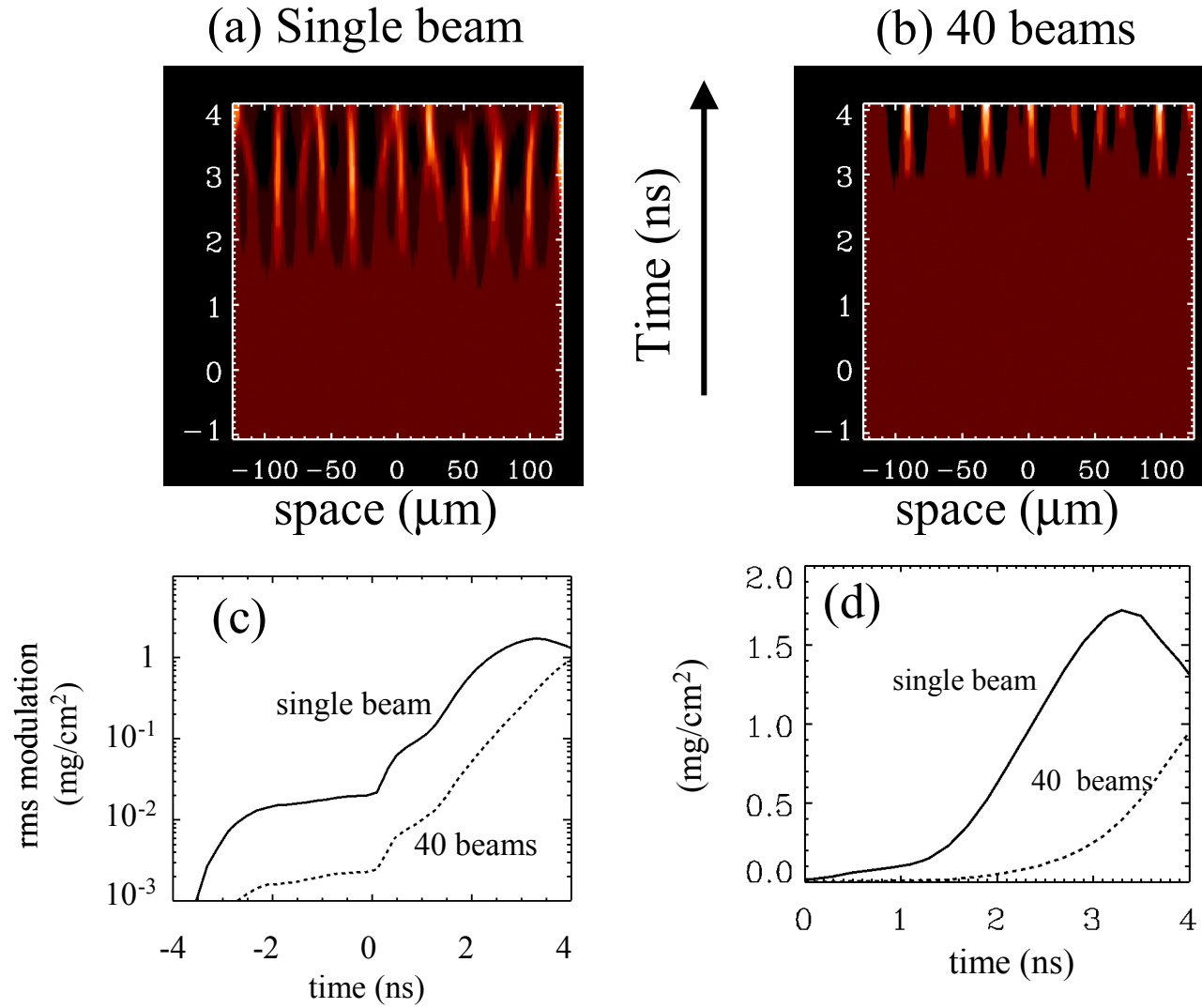


Figure 3. Two-dimensional simulations of areal mass density modulations due to RT-amplified laser imprint in uncoated CH targets: (a) single beam foot vs. (b) 40 beam foot. Higher density is depicted by the lighter colors. The growth of the RMS areal mass modulation is given on logarithmic (c) and linear plots (d) for the two cases. Reduced imprint with multiple overlapped beams is expected and observed in the simulation.

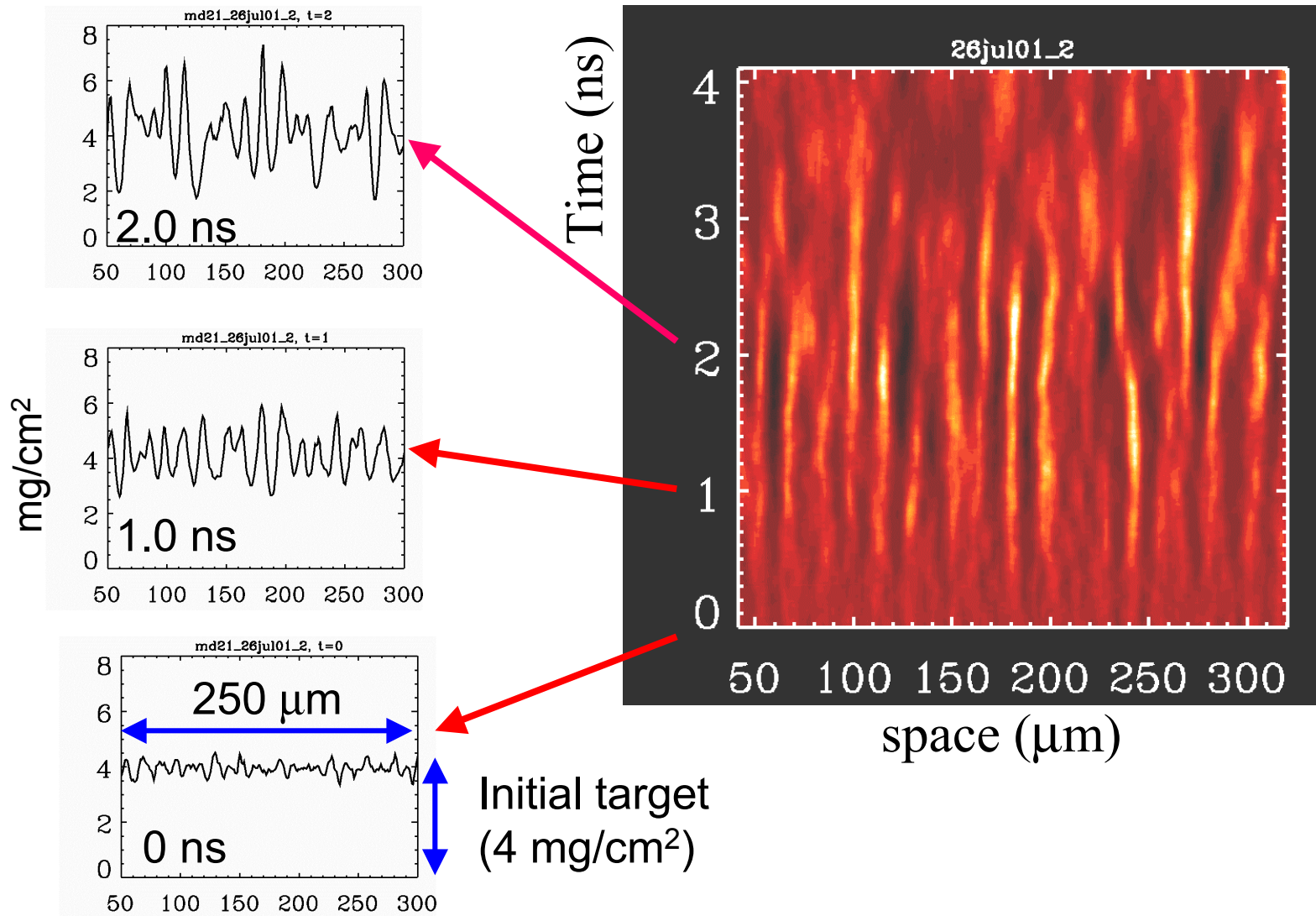


Figure 4. The RT-amplified laser imprint grows to large amplitude early in the 4-ns main pulse when using a foot pulse formed by a single laser beam onto plain plastic (CH) targets (no metal layer). The “streak camera” image shown here and for all the other figures shows the modulations in the areal mass density calculated from the x-ray transmission through the targets. The highest density (spikes) has white color; the lowest density (bubbles) has dark color.

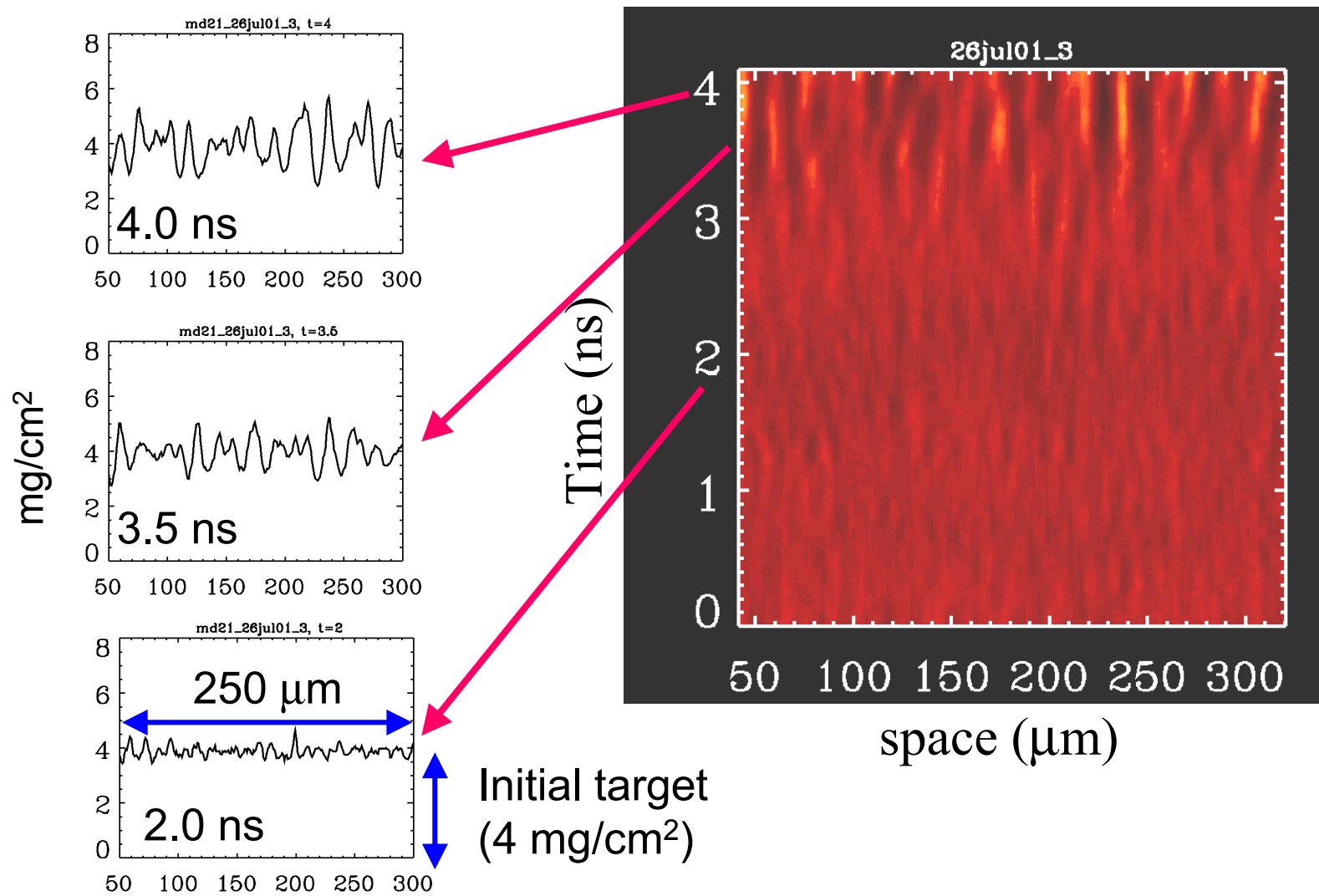


Figure 5. RT-amplified imprint is reduced with a foot pulse formed by 39 beams over that obtained with a single beam, but still reaches large amplitude near the end of the 4-ns main pulse.

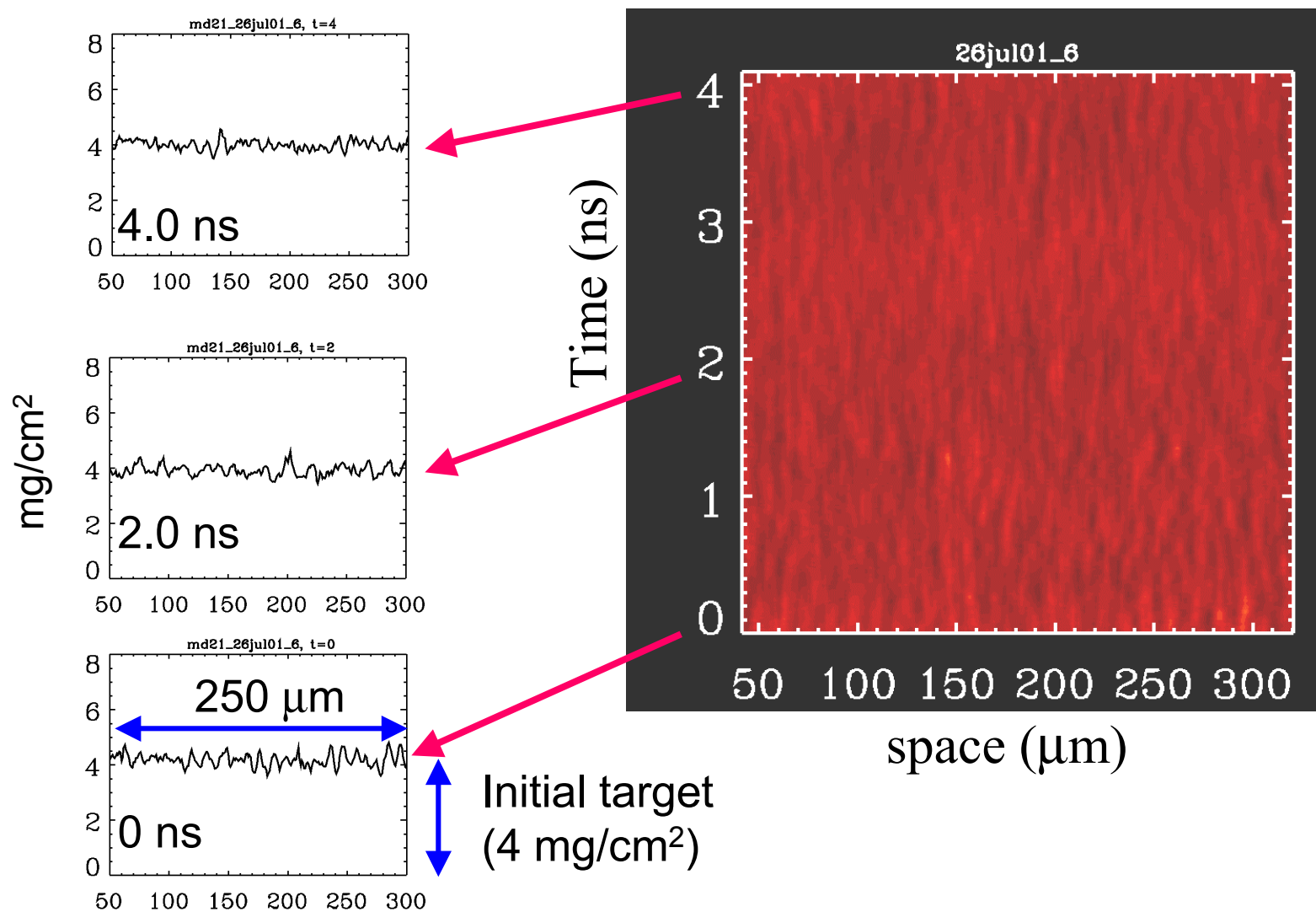


Figure 6. With a sufficient thickness of Pd as shown here (1200Å) there is no measurable RT amplified imprint even with a single beam foot.

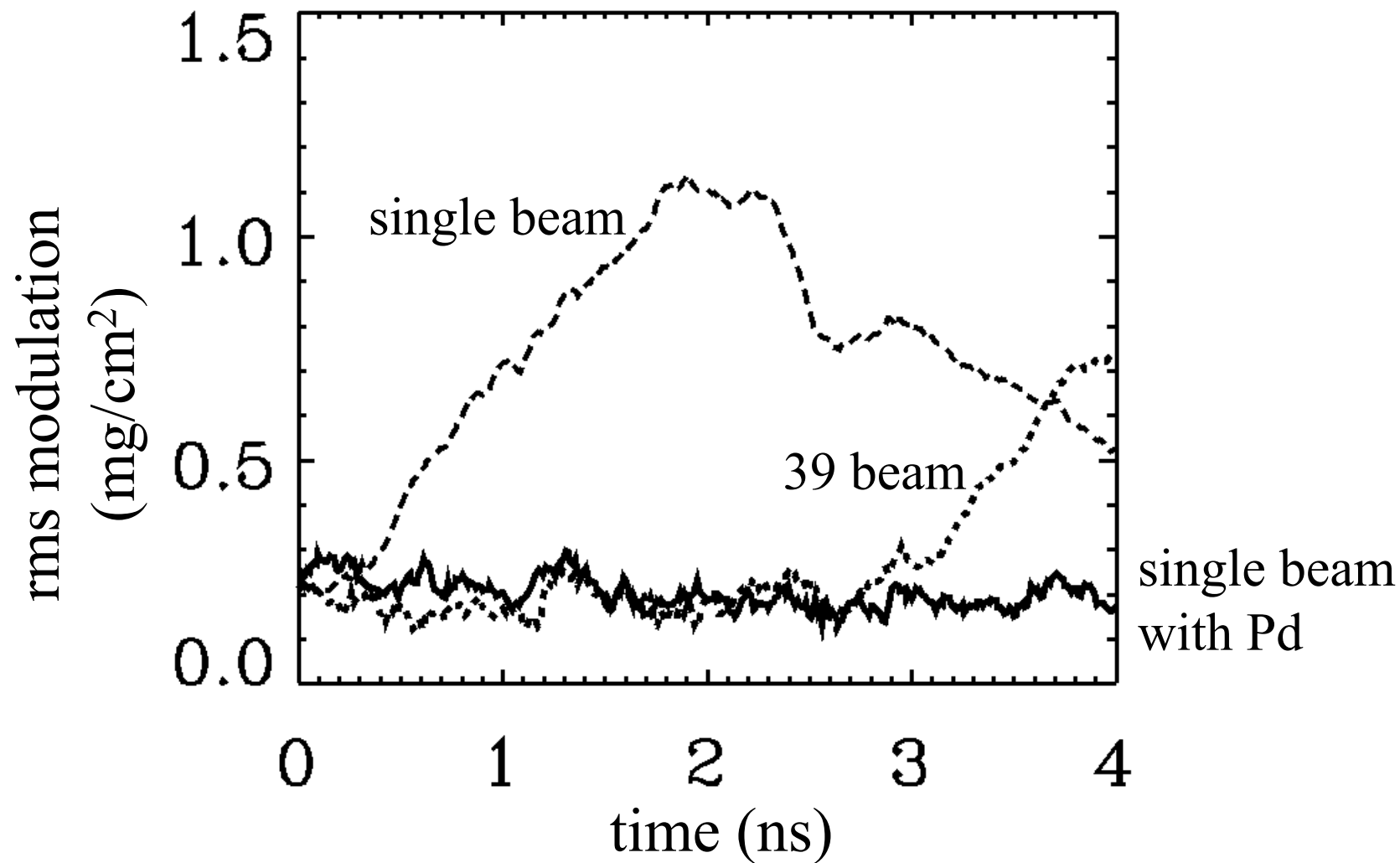


Figure 7. Experimental measurements of the growth of RMS modulations in the areal mass density with plain plastic targets with a single-beam foot (long dashed), with plain plastic and a 39-beam foot (short dashed), and a single beam foot with 1200Å Pd layer (solid) . With Pd the signal does not rise above the $\sim 0.2 \text{ mg}/\text{cm}^2$ instrumental noise by the end of the laser pulse.

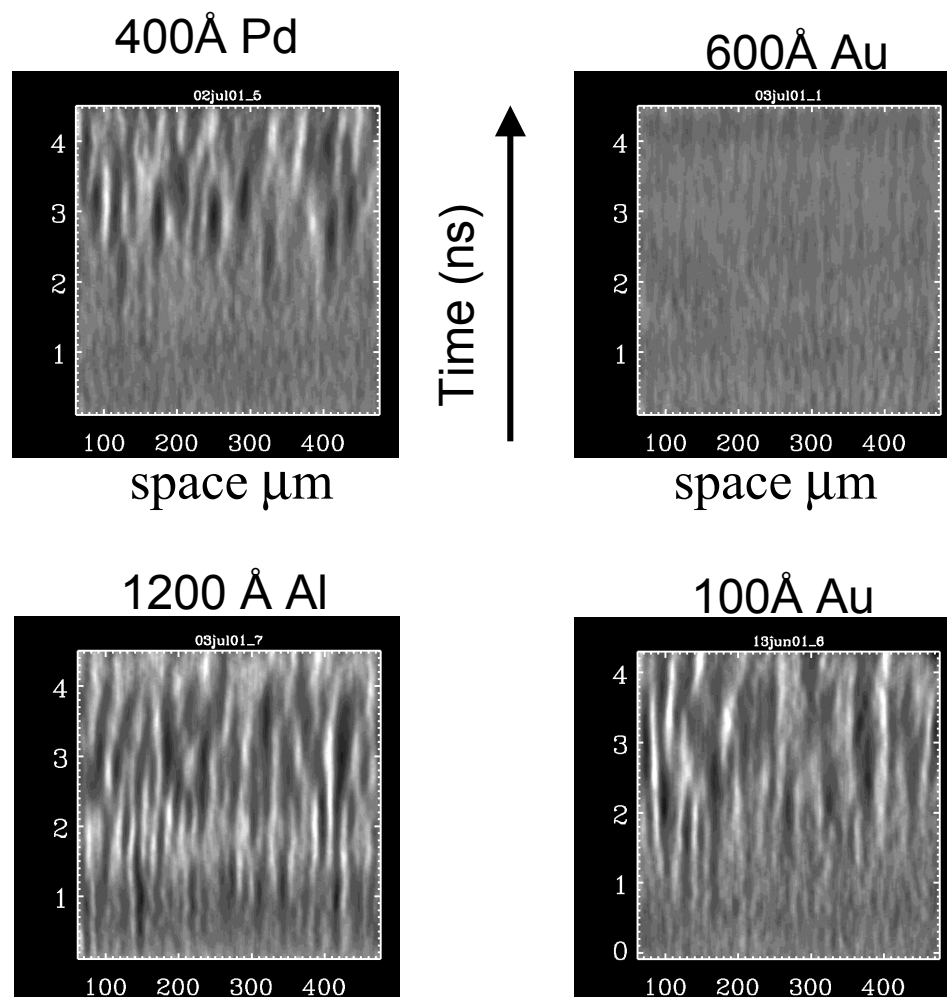


Figure 8. Gallery of results: effects of various metallic coatings on the areal mass modulation when using a single beam foot pulse. >500 Å Au layers suppressed all measurable imprint with a typical result shown for 600 Å Au. Thinner high-Z layers (100 Å Au and 400 Å Pd) allow growth of areal mass nonuniformity (although there is some suppression of single-beam imprint with the 400 Å Pd). The lower-Z 1200 Å of Al coating is totally ineffective at suppressing imprint.

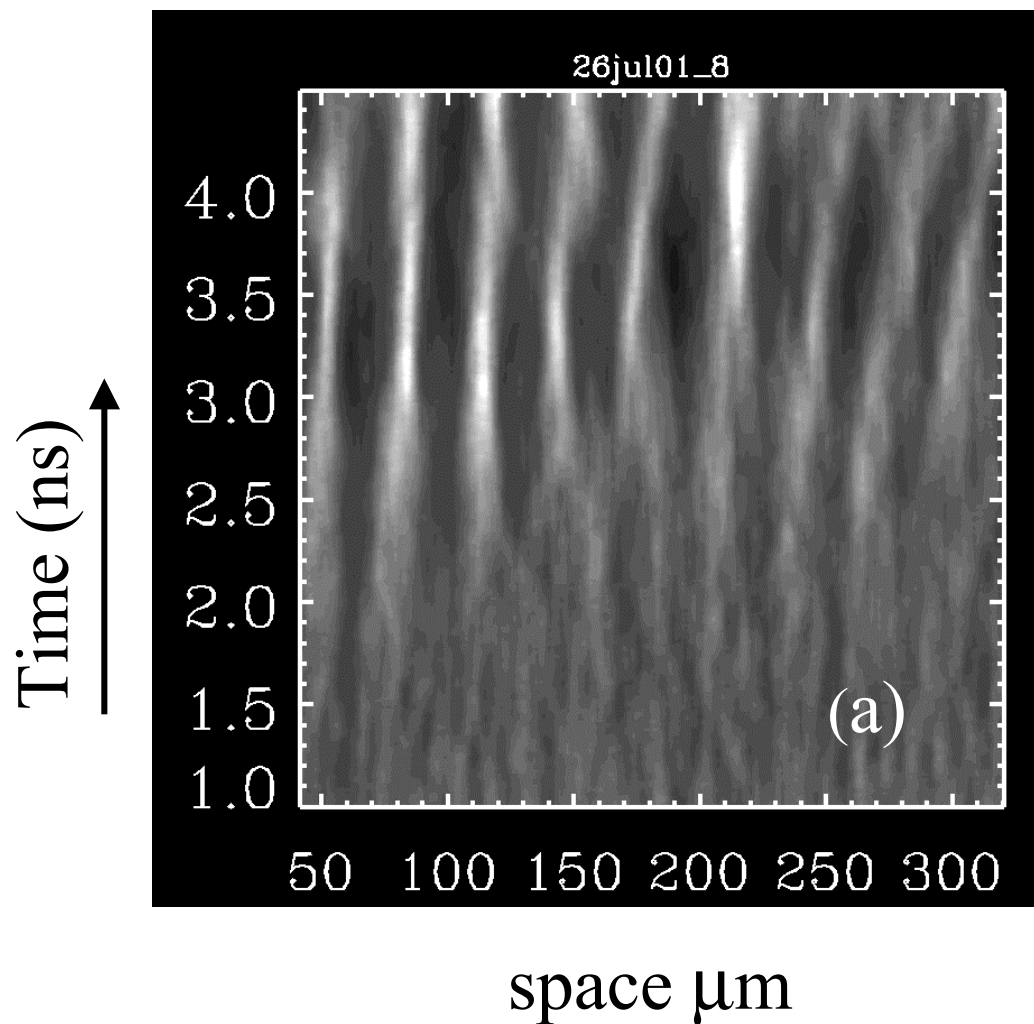


Figure 9(a). Growth in time of areal mass nonuniformity with a 39-beam foot and a 95Å Au layer. A relatively ordered structure appears with $\lambda \sim 35 \mu\text{m}$, 2 \times longer λ than typical structure with laser imprint on plain CH. X-ray backlighting with a framing camera shows that the areal mass nonuniformity such Au layers consistently evolves into a relatively ordered honeycomb like structure when using a multi-beam foot. This orderliness is lost with the effects of imprint from a single beam foot

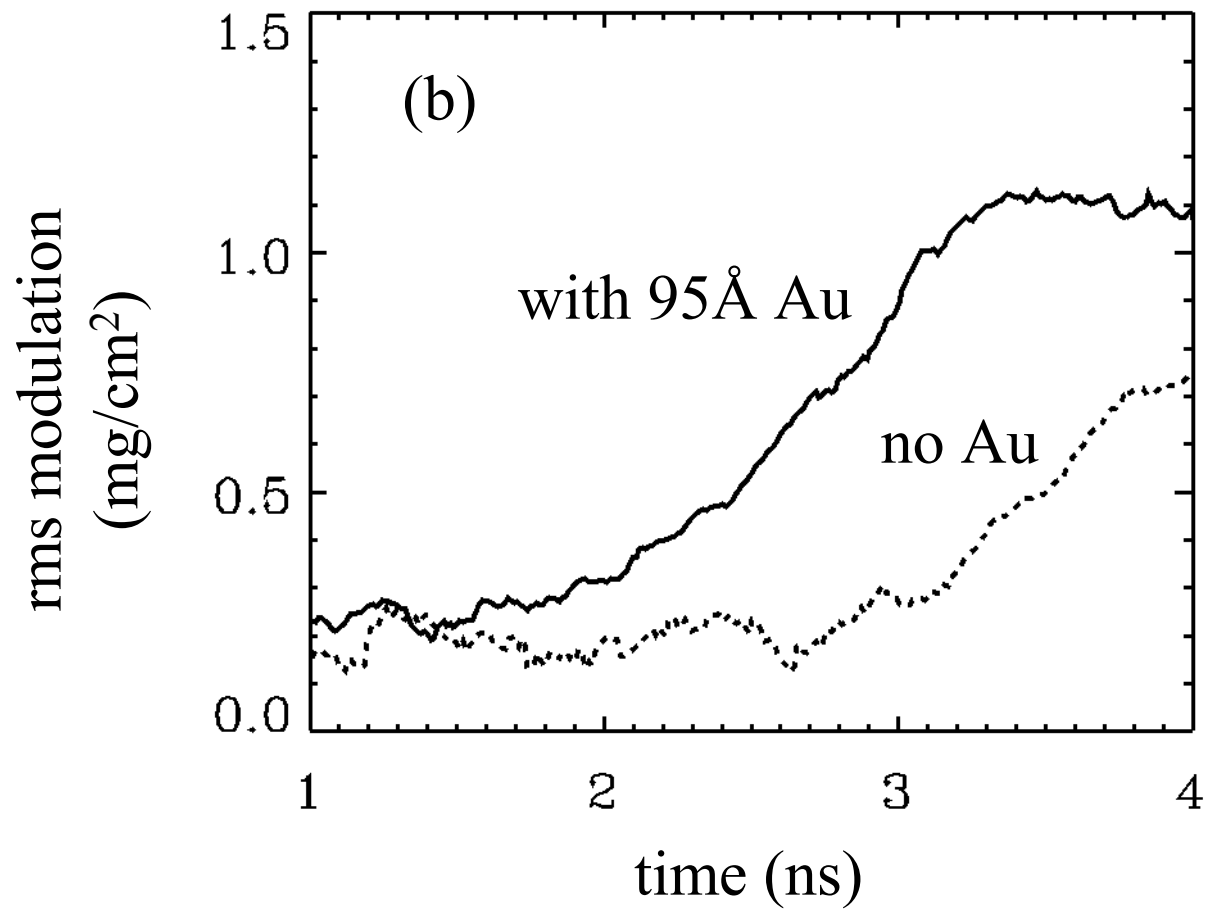


Figure 9(b). Growth in RMS areal mass nonuniformity with a 39-beam foot with and without a 95Å Au layer. The Au clearly has enhanced the growth of areal mass nonuniformity.

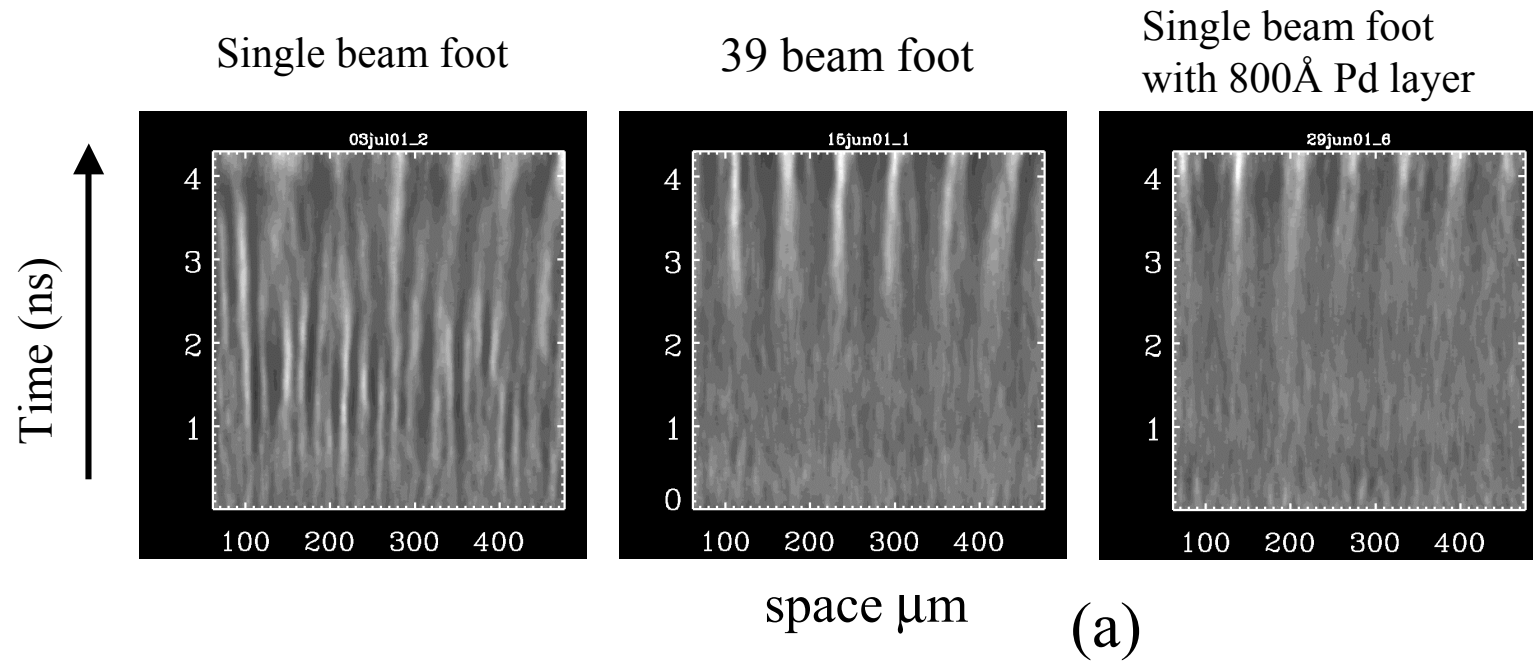


Figure 10(a). Here is shown the evolution of areal mass nonuniformity using targets with an initial $\lambda=60 \mu\text{m}$ $0.125 \mu\text{m}$ amplitude ripple on the laser illuminated surface. With a single beam foot the instability seeded by the ripple is obscured by imprint. For both the case of multi-beam foot and the case of single-beam foot with 800 \AA of Pd, most imprint is eliminated and the target-seeded $\lambda=60 \mu\text{m}$ mode predominates.

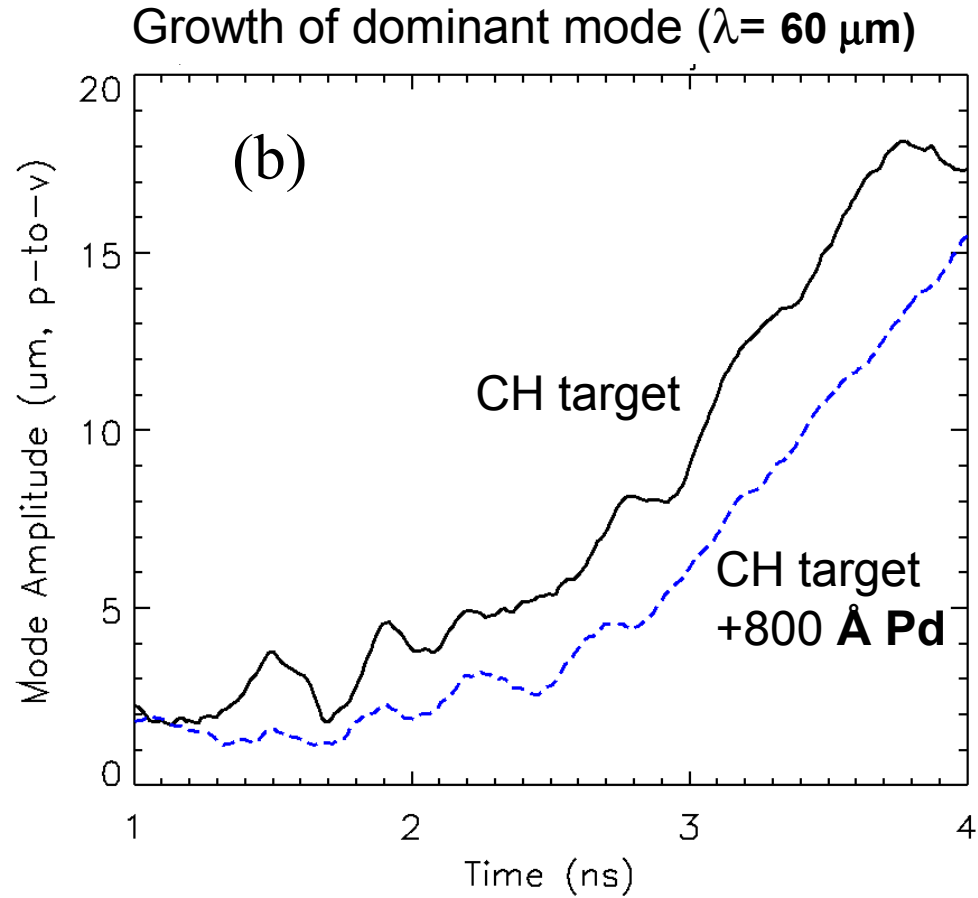


Figure 10(b). Plots of growth in the areal mass nonuniformity for the $60 \mu\text{m}$ mode is given with the same rippled targets as in (a), with a multi-beam foot, with and without a 800 \AA Pd layer. With the 800 \AA Pd layer growth is delayed, but the rate of growth during main pulse is similar to the plain CH target. Here the areal mass modulation is given as equivalent thickness of CH target at solid density.

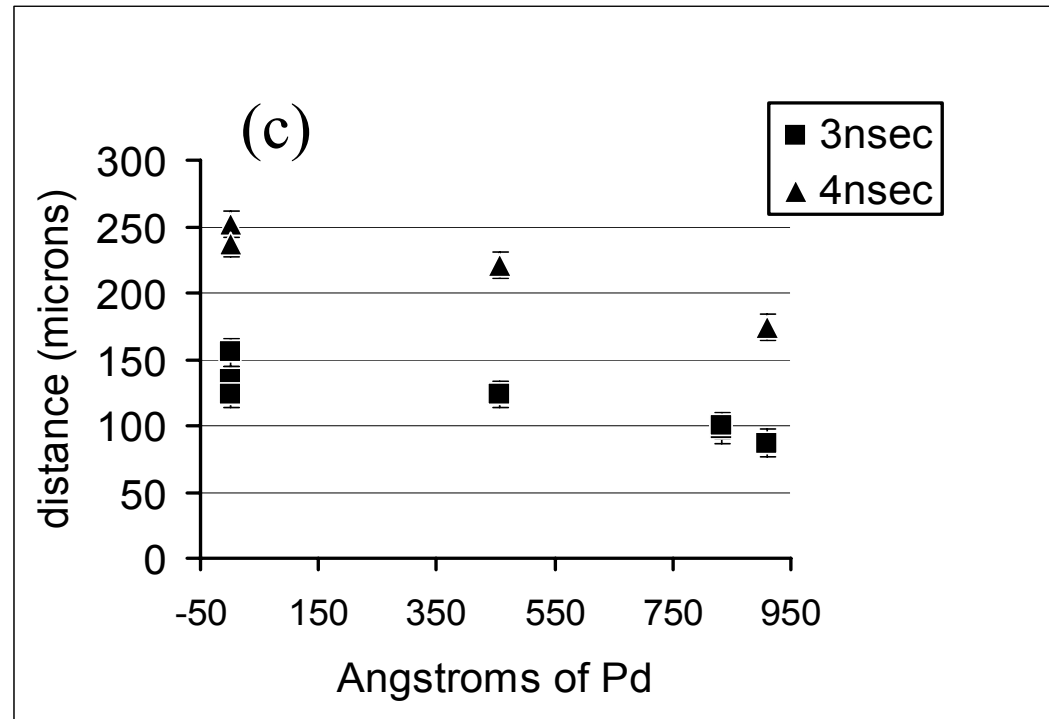


Figure 10(c). Distance that the rear surface of the laser-accelerated target traveled as a function of Pd layer thickness as determined by x-ray sidelighting (primarily 1.86 keV x-rays from Si). Shown are the position of the 20% x-ray transmission contour at 3 ns and the 50% contour at 4 ns. The displacement of the target is reduced enough with the thicker Pd to explain the short delay in the growth of the $\lambda=60\text{ }\mu\text{m}$ mode in (b).

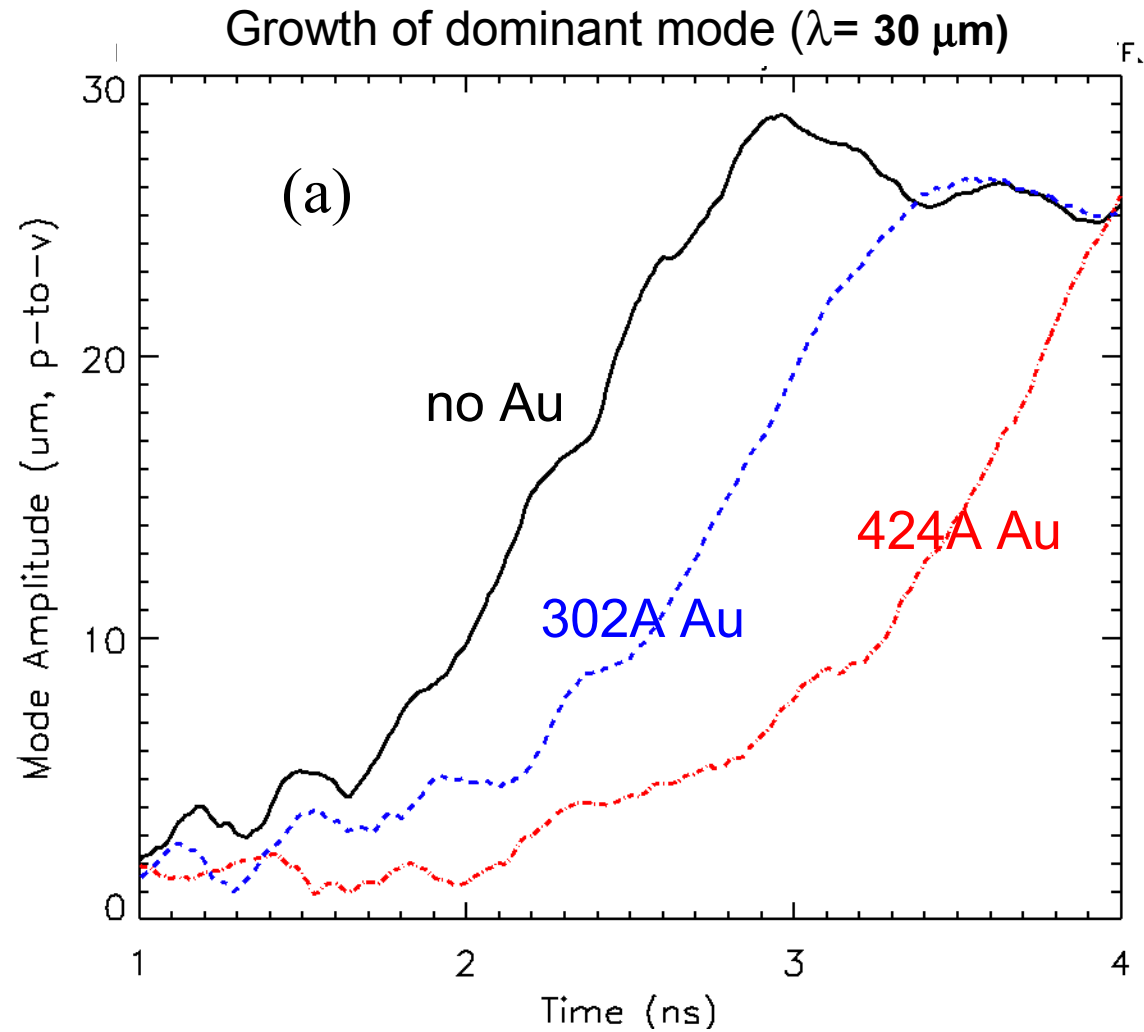


Figure 11(a). Like Pd, thicker Au layers delay growth of mass modulation from initially sinusoidally rippled targets. Here we show results with targets that have a shorter $\lambda = 30 \mu\text{m}$ sinusoidal modulation with $0.125 \mu\text{m}$ initial amplitude.

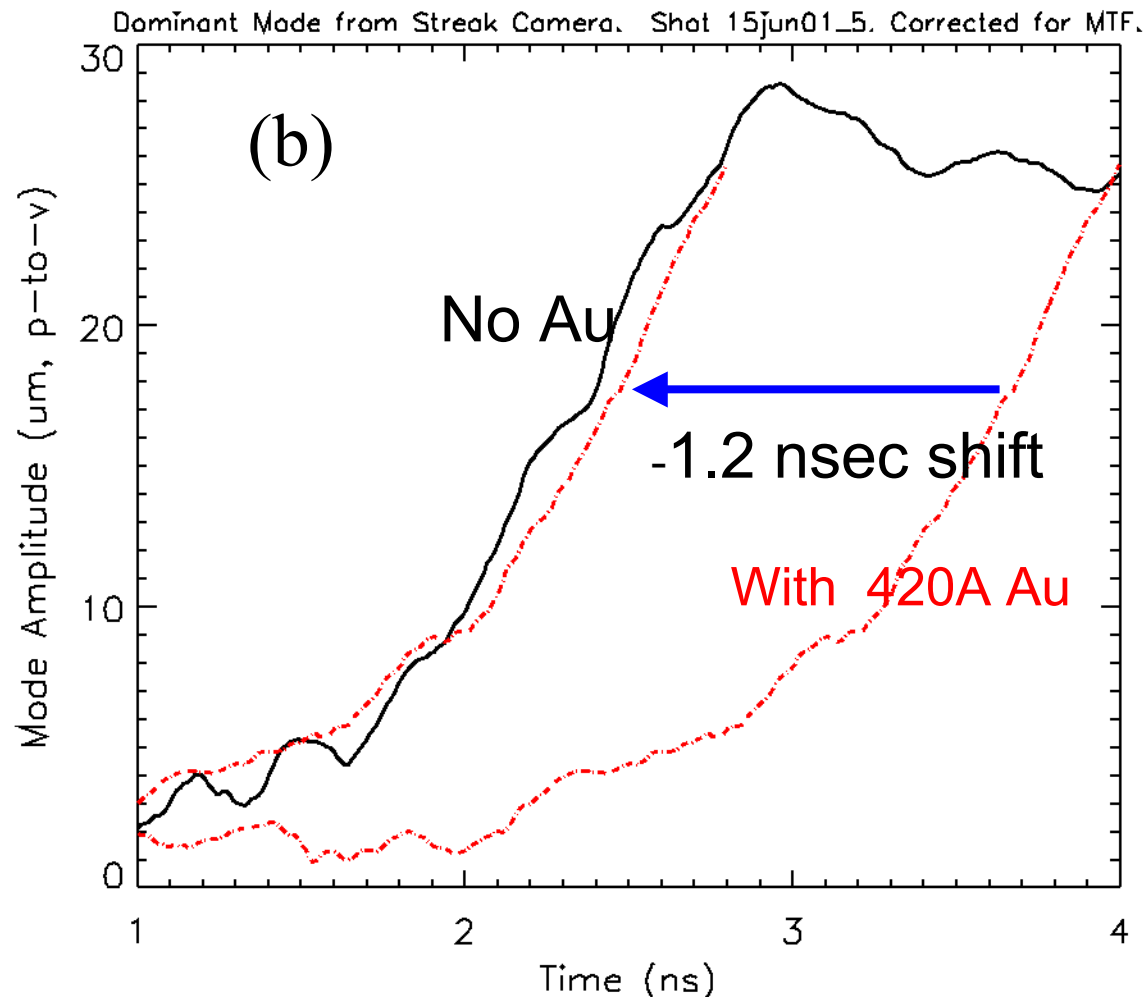


Figure 11(b). However, the rate of growth during the main pulse is similar with or without the Au layer as shown by shifting the time 1.2 ns earlier for the 420 Å Au layer.

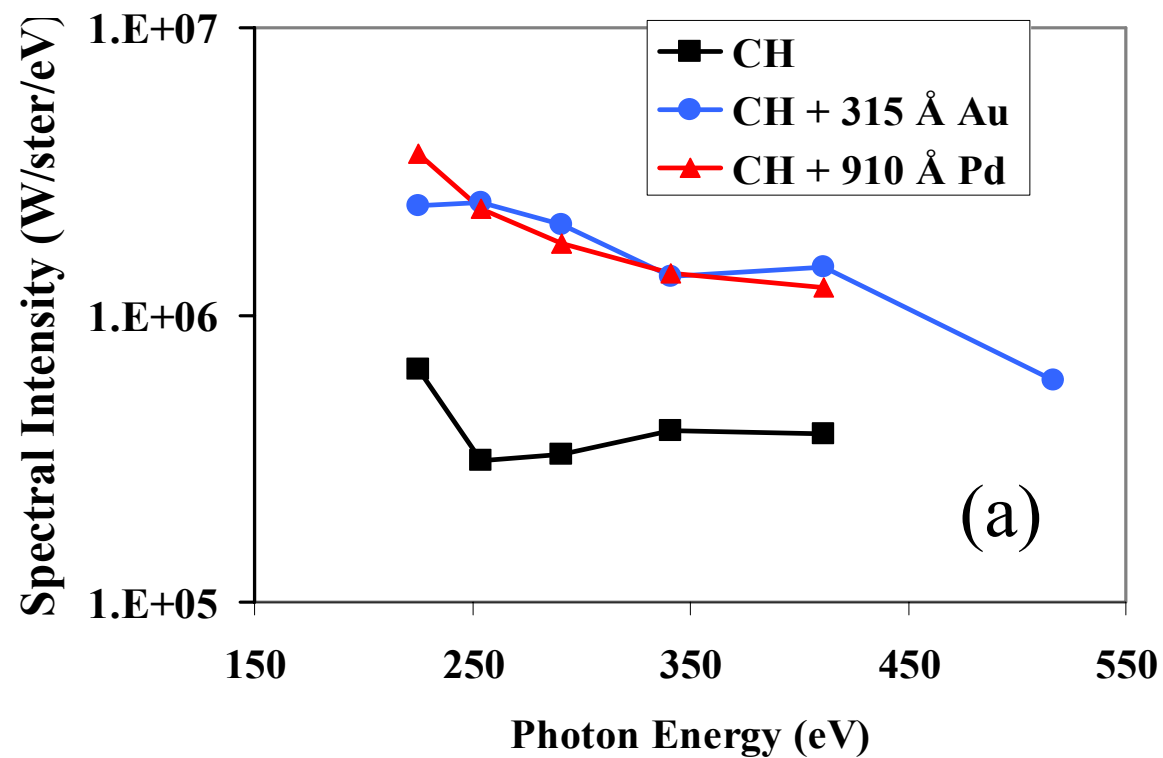


Figure 12(a). CH targets having Pd or Au layers with thickness sufficient to reduce imprint have similar emission in the soft (<500 eV) x-rays during the foot pulse.

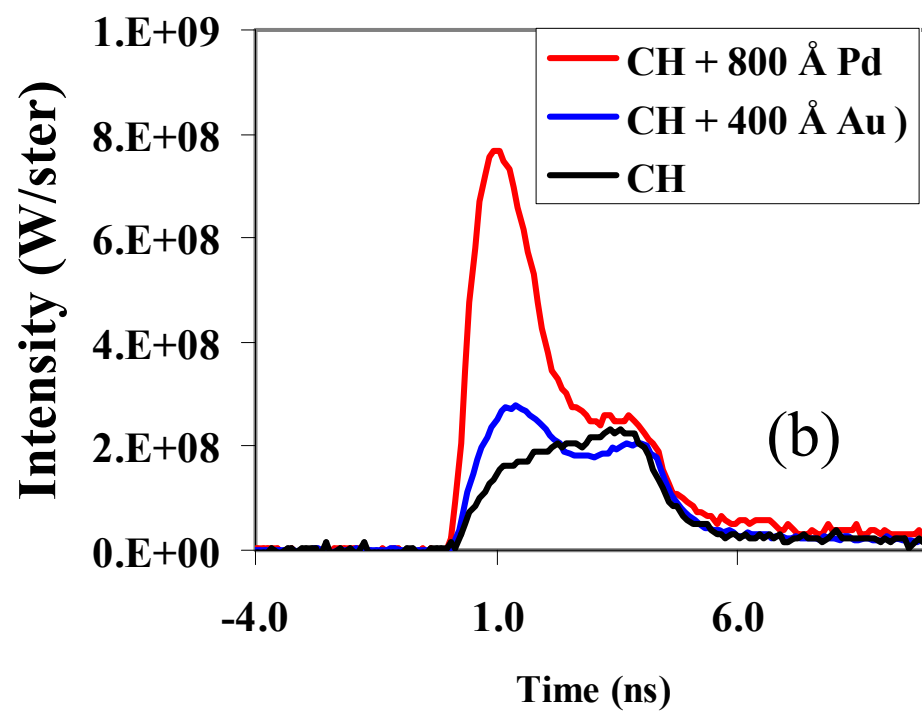


Figure 12(b). The harder x-rays (1.5-11 keV) with thin Pd and Au layers have a temporal spike, then fall to near the levels obtained with CH during the main laser pulse. The peak conversion efficiency of laser light into this band of x-rays is ~0.2% with the peak Pd layer signal.

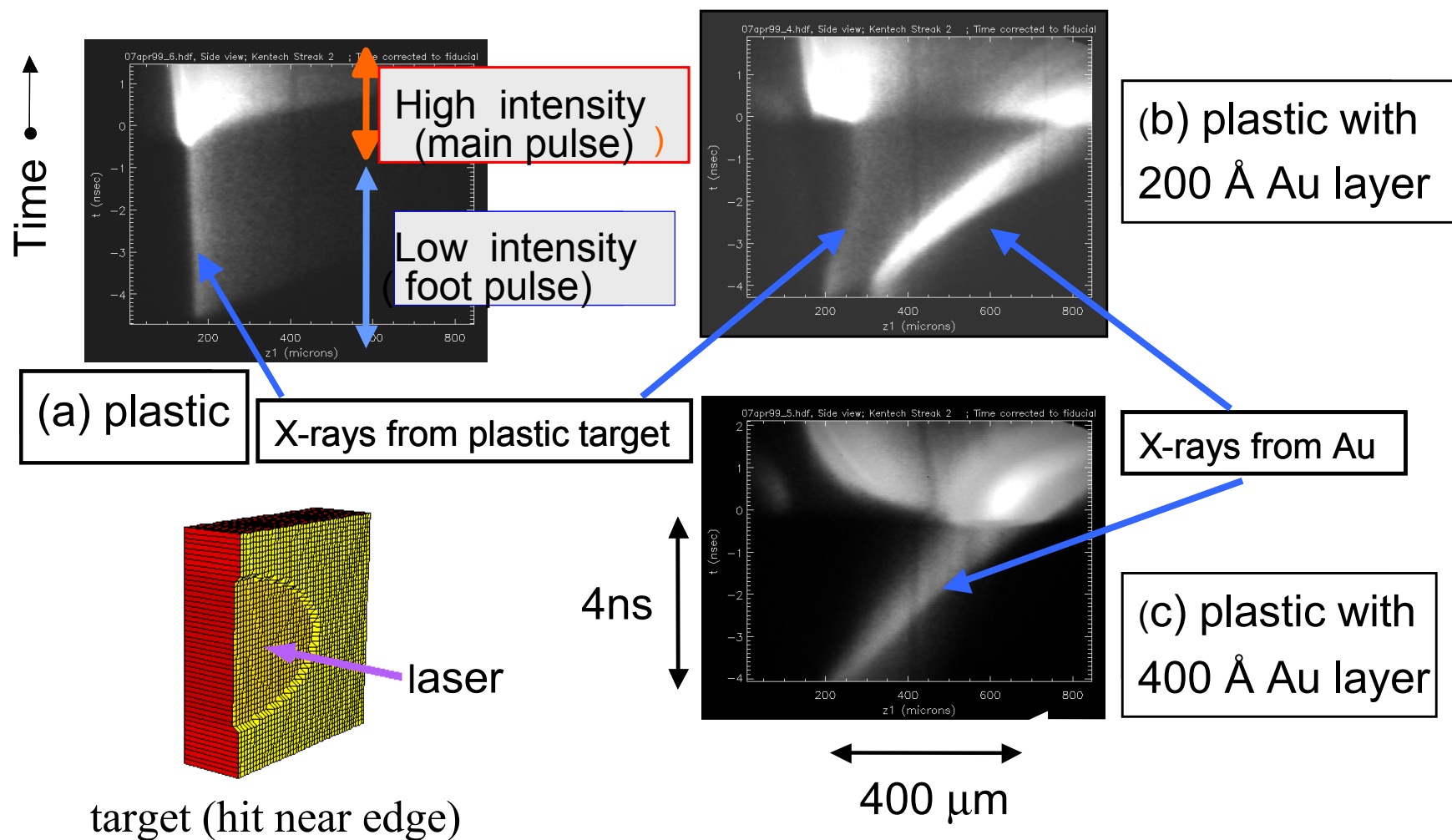


Figure 13. Side-on streak-camera views of soft x-ray emission from a plain plastic target (a) and with 200 Å (b) and 400 Å (c) Au layers. The laser has a 4 ns low intensity foot. With the thickest layer (c) there is much reduced x-ray emission from the underlying plastic target during the foot pulse, indicating that little laser light is transmitted through the gold layer. These targets are thick ($\sim 100\ \mu\text{m}$) to reduce their acceleration. The laser illumination here overlaps the target edge in order to obtain unobscured views of high-density plasma near the target as it compresses.

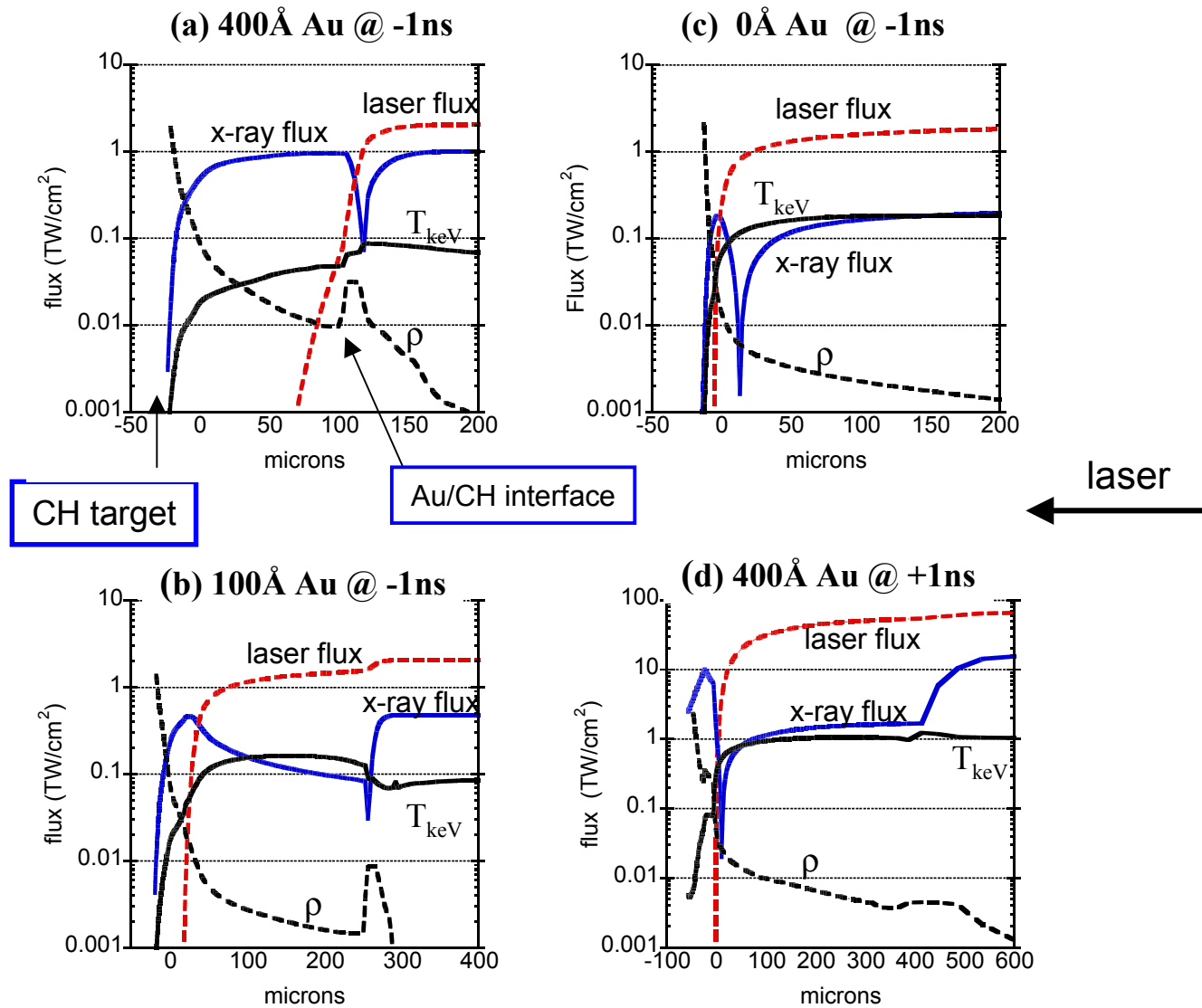


Figure 14. Calculated profiles of the laser flux, x-ray flux, temperature (T_{keV}) and mass density (ρ) near the end of the foot pulse (-1 ns) with (a) 400 Å, (b) Å 100 and (c) 0 Å Au layers on CH targets, and (d) 400 Å @+1 ns into the main pulse. During the low intensity foot pulse with a thick enough (400Å) Au layer, radiation dominates the transport of energy from the laser absorption region to the CH target, most of the laser light is absorbed by the Au layer. Later, with the higher intensity main pulse, most of the laser light is transmitted though the Au layer.

1D implosion using NRL FAST code

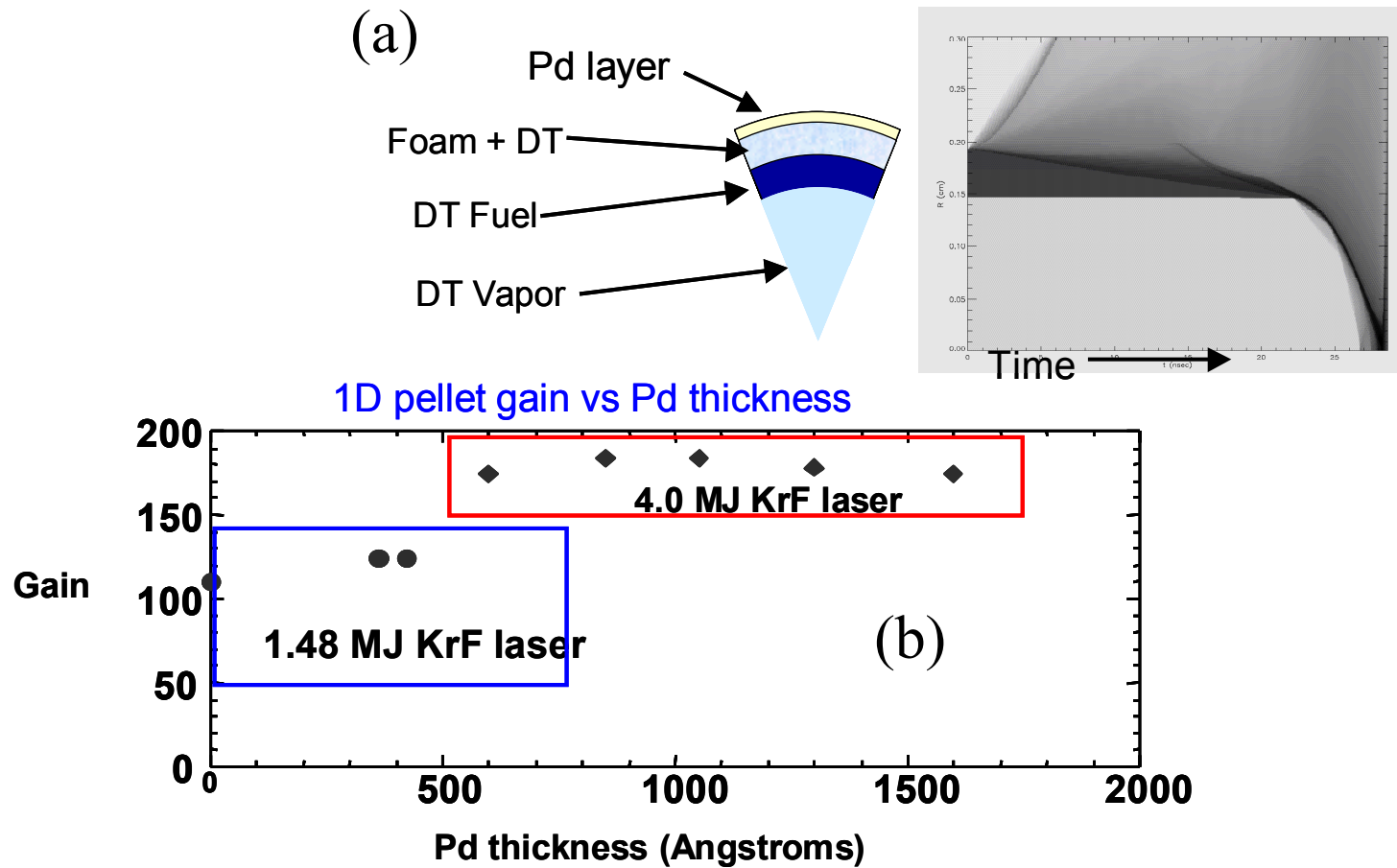


Figure 15. (a) Implosion of a pellet with a Pd layer as calculated from the 1-D FAST code. **(b)** Calculations of pellet gain (with a lower and higher energy KrF laser) using the 1-D code predict that gain is not degraded by Pd layers thick enough to suppress laser imprint.